# Microwave-assisted hydrothermal synthesis of $Ag_2(W_{1-x}Mo_x)O_4$ heterostructures: Nucleation of Ag, morphology, and photoluminescence properties

M.D.P. Silva [a], R.F. Gonçalves [b,*], I.C. Nogueira [c], V.M. Longo [d], L. Mondoni [a], M.G. Moron [a], Y.V. Santana [e], E. Longo [f]

[a] LIEC-Universidade Federal de São Carlos, Rod. Washington Luis, km 235, São Carlos, SP CEP: 13565-905, Brazil
[b] UNIFESP—Universidade Federal de São Paulo, Rua Prof. Artur Riedel, 275, Diadema, SP CEP 09972-270, Brazil
[c] IFMA — Instituto Federal do Maranhão, Avenida Getúlio Vargas, no 04 — Monte Castelo, São Luís, MA CEP 65030-005, Brazil
[d] USP — Universidade de São Paulo, Av. Trabalhador São-Carlense, 400 — Arnold Schimidt, São Carlos, SP CEP 13566-590, Brazil
[e] UTFPR—Universidade Tecnológica Federal do Paraná, Av. Alberto Carazzai, 1640, Cornélio Procópio, PR CEP 86300-000, Brazil
[f] LIEC-IQ-Universidade Estadual Paulista, P.O. Box 355, Araraquara, SP CEP 14801-907, Brazil

## ARTICLE INFO

## ABSTRACT

$Ag_2W_{1-x}Mo_xO_4$ (x = 0.0 and 0.50) powders were synthesized by the co-precipitation (drop-by-drop) method and processed using a microwave-assisted hydrothermal method. We report the real-time in situ formation and growth of Ag filaments on the $Ag_2W_{1-x}Mo_xO_4$ crystals using an accelerated electron beam under high vacuum. Various techniques were used to evaluate the influence of the network-former substitution on the structural and optical properties, including photoluminescence (PL) emission, of these materials. X-ray diffraction results confirmed the phases obtained by the synthesis methods. Raman spectroscopy revealed significant changes in local order–disorder as a function of the network-former substitution. Field-emission scanning electron microscopy was used to determine the shape as well as dimensions of the $Ag_2W_{1-x}Mo_xO_4$ heterostructures. The PL spectra showed that the PL-emission intensities of $Ag_2W_{1-x}Mo_xO_4$ were greater than those of pure $Ag_2WO_4$, probably because of the increase of intermediary energy levels within the band gap of the $Ag_2W_{1-x}Mo_xO_4$ heterostructures, as evidenced by the decrease in the band-gap values measured by ultraviolet–visible spectroscopy.

## 1. Introduction

In recent years, strategies for fabricating low-dimensional structures of tungstate and molybdate compounds have received much attention owing to the novel geometry-dependent properties of these compounds and their potential applications in various fields [1]. In particular, silver molybdate ($Ag_2MoO_4$) and silver tungstate ($Ag_2WO_4$) exhibit excellent electrical and optical properties; hence, they are ideal for application in sensors, optical devices, as well as in photodegradation and catalytic processes; they are also used as antibacterial agents and energy storage materials [2,3].

The properties of such compounds are directly determined by their structure, morphology, and dimension. Therefore, a fundamental understanding of the structural evolution and features of these compounds is essential before producing them by controlled synthesis; in particular, achieving precise control over their parameters is an important goal.

Previous research into the evolution and features of tungstate and molybdate compounds used techniques that require high temperatures and long processing times [4,5]. Lately, the microwave-assisted hydrothermal (MAH) method has received special attention owing to its interesting advantages, which include rapid, uniform, and selective heating; reduced processing costs; better production quality; and the possibility of creating new, technologically important materials [6].

Recently, we used an electron beam to demonstrate the in situ growth of Ag nanofilaments from $\alpha$-$Ag_2WO_4$ crystals [7,8]. An external stimulus, such as an accelerated electron beam in field-emission scanning electron microscopy (FE-SEM), is capable of initiating the nucleation and growth of Ag filaments.

Some studies have been conducted to explore the properties of silver tungstate [9,10], which exhibits three different structures: $\alpha$-orthorhombic [10], $\beta$-hexagonal [11], and $\gamma$-cubic [12]. Pang et al. [13] prepared $Ag_2WO_4$ particles with good antimicrobial activity. Cavalcante et al. [14] obtained hexagonal, rod-like, elongated silver tungstate ($\alpha$-$Ag_2WO_4$) microcrystals and studied their optical properties. Recently, a new ozone gas sensor based on $\alpha$-$Ag_2WO_4$ nanorod-like structures was designed, and electrical resistance measurements proved the efficiency of the $Ag_2WO_4$ nanorods [15]. The sensor showed good

* Corresponding author at: Walter Brendel Centre of Experimental Medicine, Ludwig-Maximilians-Universität München, Marchioninistr. 27, D-81377 München, Germany.
E-mail address: rosanaf.gon@gmail.com (R.F. Gonçalves).

sensitivity even for a low ozone concentration (80 ppb), fast response, and short recovery time at 300 °C.

Silver molybdates have also received considerable attention owing to their chemical stability at elevated temperatures, as well as their applications in optical and electrochemical devices [16]. $Ag_2MoO_4$ can be found in two forms: $\alpha$-$Ag_2MoO_4$, which has a tetragonal structure, and $\beta$-$Ag_2MoO_4$, which is cubic with a spinel structure. The $\alpha$-phase irreversibly transforms to the $\beta$-phase upon heating above the ambient temperature. These compounds have been used in applications such as catalysis, gas sensing, and surface-enhanced Raman scattering techniques [6].

In this paper, we discuss the structure, optical properties, and growth of silver filaments on $Ag_2W_{1-x}Mo_xO_4$ (x = 0.0 and 0.50) powders synthesized via the MAH method.

## 2. Experimental details

### 2.1. Synthesis of $Ag_2W_{1-x}Mo_xO_4$ crystals

$Ag_2W_{1-x}Mo_xO_4$ crystals (x = 0.0 and 0.5) were synthesized by the co-precipitation (drop-by-drop) method. The precursors were 0.001 mol of sodium tungstate dihydrate ($Na_2WO_4.2H_2O$) (99.5% purity, Aldrich), 0.001 mol of sodium molybdate dihydrate ($Na_2MoO_4 \cdot 2H_2O$) (99.5% purity, Aldrich), and 0.001 mol of silver nitrate (99% purity, Aldrich). A Masterflex 77240-10 L/S compact variable-speed pump was used to drip 30 mL of an aqueous solution of $Ag^+$ ions at a flow rate of 10 mL $min^{-1}$ into 50 mL of an aqueous solution containing $WO_4^{2-}$ and $MoO_4^{2-}$ ions (at 368 K) in a 250 mL beaker. For all systems, the temperature was maintained at 343 K for 30 min, and the agitation rate in the IKA C-MAG HS-7 magnetic stirrer was 700 r $min^{-1}$.

After precipitation, the suspensions were transferred to a Teflon autoclave, sealed, and placed in the MAH system (2.45 GHz, maximum power 800 W). The reaction mixture was heated at 140 °C for 1 h. Then, the autoclave was naturally cooled to room temperature. Finally, the product was washed with deionized water several times and dried at 50 °C for 6 h.

### 2.2. Characterization of $Ag_2W_{1-x}Mo_xO_4$ crystals

The synthesized crystals were structurally characterized with X-ray diffraction (XRD) (D/Max-2500PC diffractometer (Rigaku, Japan)) using Cu-K$\alpha$ radiation ($\lambda$ = 1.5406 Å) in a 2$\theta$ range from 10° to 70° with a scanning rate of 1° $min^{-1}$. The FT-Raman spectra were recorded (Bruker-RFS 100 (Germany)). The Raman spectra were obtained using a 1064-nm line with a Nd:YAG laser having a maximum output power of 100 mW in the range of 50–1000 $cm^{-1}$. The morphologies of the $Ag_2W_{1-x}Mo_xO_4$ crystals were observed with an FE-SEM (Carl Zeiss, model Supra 35-VP (Germany)) operated at 6 kV. Ultraviolet–visible (UV–vis) spectra were recorded using a Varian spectrophotometer (Varian, Cary 5G model) in the diffuse reflectance mode. PL measurements were performed using a Monospec 27 monochromator (Thermal Jarrel Ash, USA) coupled to a R446 photomultiplier (Hamamatsu, Japan). A krypton ion laser (Coherent Innova 90 K, USA) ($\lambda$ = 350.7 nm) was used as the excitation source, with the output power maintained at 500 mW. The laser beam was passed through an optical chopper, and its maximum power on the sample was maintained at 40 mW. All PL measurements were performed at room temperature.

## 3. Results and discussion

### 3.1. XRD analysis

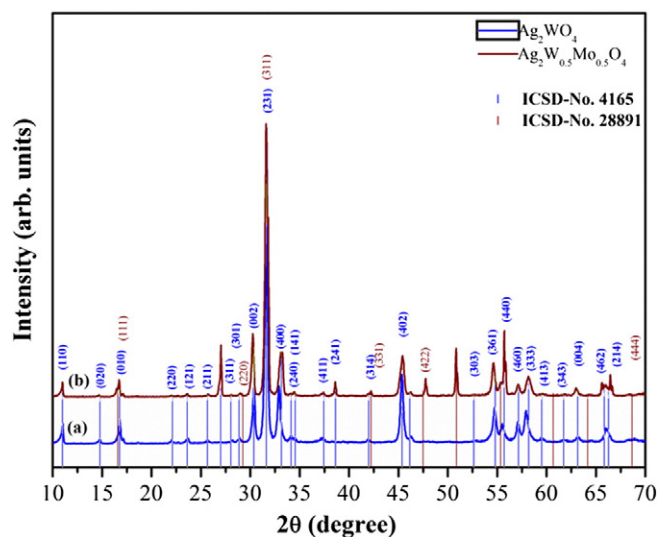Fig. 1 shows typical XRD patterns of the $Ag_2(W_{1-y}Mo_x)O_4$ crystals with (a) x = 0.0 and (b) x = 0.50 synthesized at 140 °C for 1 h by the MAH method.



**Fig. 1.** XRD patterns of $Ag_2(W_{1-x}Mo_x)O_4$ crystals with (a) x = 0 and (b) x = 0.50 synthesized at 140 °C for 1 h by the MAH method. Vertical lines indicate the position and intensity relative to the ICSD card No. 4165 for the $\alpha$-$Ag_2WO_4$ phase and card No. 28891 for the $\beta$-$Ag_2MoO_4$ phase.

The sharp and well-defined diffraction peaks indicate a high degree of crystallinity; i.e., all precipitated crystals are structurally ordered at long ranges. The XRD patterns illustrated in Fig. 1(a) reveal that the diffraction peaks for $\alpha$-$Ag_2WO_4$ crystals with x = 0.0 are monophasic and can be indexed to the orthorhombic structure with space group $Pn2n$, which is in agreement with the Inorganic Crystal Structure Database (ICSD) No. 4165 [17]. However, Fig. 1(b) shows that the diffraction peaks for $Ag_2(W_{1-x}Mo_x)O_4$ (with x = 0.50) crystals present two phases that can be indexed to the orthorhombic structure with space group $Pn2n$ for the $\alpha$-$Ag_2WO_4$ phase (ICSD No. 4165) and to the cubic structure with space group $Fd-3\,m$ for the $\beta$-$Ag_2MoO_4$ phase (ICSD No. 28891).

Fig. 1 shows a displacement of the diffraction peaks, which leads us to believe that there is some substitution of tungsten ions by ions of molybdenum. To quantify the actual concentration of molybdenum in each phase and to determine if solid solutions were formed, Rietveld refinement was performed on the synthesized crystals.

### 3.2. Rietveld refinement analysis

Fig. 2 shows observed and calculated Rietveld refinement plots for $Ag_2(W_{1-x}Mo_x)O_4$ crystals with different compositions (x = 0.0 and 0.50) synthesized at 140 °C for 1 h by the MAH method.

In this work, the Rietveld refinements were performed through the general structure analysis (GSAS) program [18]. Space groups $Pn2n$ and $Fd-3\,m$ were assumed for the orthorhombic and cubic ($Ag_2WO_4$) structures, respectively, and they were adjusted to ICSD No. 50821 [19] and ICSD No. 173120 [20]. In these analyses, the scale factor, background, lattice-constant shifts profile half-width parameters (u, v, w), isotropic thermal parameters, lattice parameters, strain anisotropy factor, preferred orientation, and occupancy and atomic functional positions served as the refined parameters. The background was corrected using a Chebyshev polynomial of the first kind. The peak profile function was modeled using a convolution of the Thompson–Cox–Hastings pseudo-Voigt (pV-TCH) function [21] with the asymmetry function described by Finger [22], which accounts for asymmetries due to axial divergence. Stephens' model [23] was used to account for the anisotropy in the half width of the reflections. The results we obtained from the Rietveld refinements are listed in Tables 1 and 2.

Table 1 indicates that there are low deviations in certain statistical parameters ($R_{wp}$, $R_p$, $R_{Bragg}$, and $\chi^2$), indicating that structural refinement and numerical results are of a good quality. In this table, it can
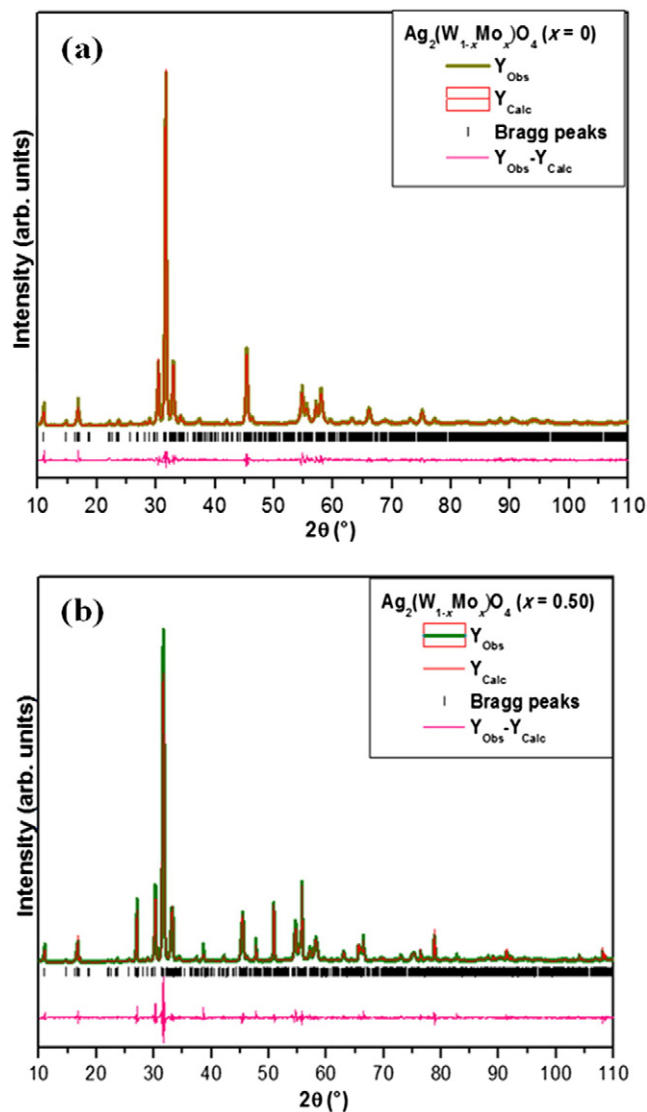
**Fig. 2.** Rietveld refinements of the $Ag_2(W_{1-x}Mo_x)O_4$ crystals with (a) x = 0 and (b) x = 0.50.

be seen that a single $Ag_2WO_4$ phase is formed for the composition with x = 0.0. For the composition with x = 0.50, we can observe two solid solutions. The composition (x = 0.50) showed 67.15% of $Ag_2(W_{0.92}Mo_{0.08})O_4$ solid solution with an orthorhombic structure and *Pn2n* space group, and 32.85% of $Ag_2(W_{0.08}Mo_{0.92})O_4$ solid solution with a cubic structure and *Fd-3 m* space group. These results reveal the formation of a heterostructure.

Table 2 lists the lattice parameters and unit-cell volumes obtained by the Rietveld refinement analyses for $Ag_2(W_{1-x}Mo_x)O_4$ (x = 0.0 and 0.50) crystals. The variations in lattice parameters and volume indicate that there are distortions in the unit cell caused by the replacement of $WO_6$ clusters by $MoO_6$ clusters and vice versa in the formation of solid solutions.

## 3.3. Analysis of micro-Raman spectra

Raman spectroscopy can be employed as a probe to investigate the degree of short-range structural order–disorder in materials [24,25]. Indeed, this technique provides information on the structure of the molecule, as changes in the Raman spectral profile may indicate structural transformations from one phase to another. The Raman spectrum of pure $Ag_2WO_4$ crystals synthesized using the MAH method is depicted in Fig. 3(a), where we can experimentally detect seven Raman-active modes: 82 cm$^{-1}$ ($B_{1g}$ mode), 202 cm$^{-1}$ ($A_{1g}$ mode), 301 cm$^{-1}$ ($A_{2g}$ mode), 660 cm$^{-1}$ ($B_{1g}$ mode), 733 cm$^{-1}$ ($B_{1g}$ mode), 799 cm$^{-1}$ ($A_{2g}$ mode), and 879 cm$^{-1}$ ($A_{1g}$ mode).

An important feature of the crystals is the more pronounced structural local order presented by the lattice in the form of $[WO_6]$ clusters (879 cm$^{-1}$), as opposed to the lattice modifier assigned to $[AgO_y]$ clusters [8]. Internal vibrations are associated with movements inside the $[WO_6]$ molecular group, which are revealed as peaks with Raman-active internal modes of octahedral $[WO_6]$ clusters.

Fig. 3(b) depicts the FT-Raman spectrum of the $Ag_2W_{0.50}Mo_{0.50}O_4$ powders, where the peaks can be assigned to the heterostructure. All of the peaks ascribed to $Ag_2WO_4$ (Fig. 3(a)), except for the most intense peak that was shifted to a lower wave number, remain on the spectrum. The shift of the most intense peak is probably due to the mixed-phase formation, as observed in the XRD pattern in Fig. 1. Indeed, new vibrational modes ascribed to $Ag_2MoO_4$ appear, suggesting that a new compound containing a two-phase mixture, or a heterostructure, has formed.

Therefore, only five Raman-active vibrational modes are expected for $AgMoO_4$ crystals, as expressed by Eq. (1):

$$\Gamma_{(Raman)} = A_{1g} + E_g + 3T_{2g}. \tag{1}$$

In addition to the vibrational modes associated with $Ag_2WO_4$, Fig. 3(b) shows that the peak at 867 cm$^{-1}$ ($A_{1g}$ mode) may be attributed to the symmetric stretching of the Mo–O bond in the $MoO_4$ units, whereas the peak at 756 cm$^{-1}$ ($T_{2g}$ mode) is assigned to the bridging of Mo–O–Ag bonds, and the peaks in the 200–400 cm$^{-1}$ range ($E_g$ and $T_{2g}$ mode) correspond to the bending modes of the crystal. However, one $T_{2g}$ mode related to the mobility of O atoms into the structure is not experimentally detectable. These findings are in good agreement with the existing literature [26,17,27].

It is notable that the Raman spectra of the synthesized crystals exhibited broad vibrational modes, indicating short-range structural disorder. This characteristic can be related to the very rapid kinetics of the synthesis conditions in the MAH method. It is well known that the physical and chemical properties of materials are strongly correlated with some structural factors: mainly the structural order–disorder in the lattice. Breaking the symmetry processes of these clusters with distortions, breakings, and tilts creates a huge number of different structures and subsequently different material properties related to local (short), intermediate, and long-range structural order–disorder [28,29].

## 3.4. Ultraviolet–visible absorption spectroscopy analysis

The optical band-gap energy ($E_{gap}$) was calculated using the method proposed by Kubelka and Munk [30]. This method uses a transformation

**Table 1**
Phase compositions and statistical parameters of quality obtained by Rietveld refinement for the $Ag_2(W_{1-x}Mo_x)O_4$ crystals with (x = 0 and 0.50) synthesized at 140 °C for 1 h by the MAH method.

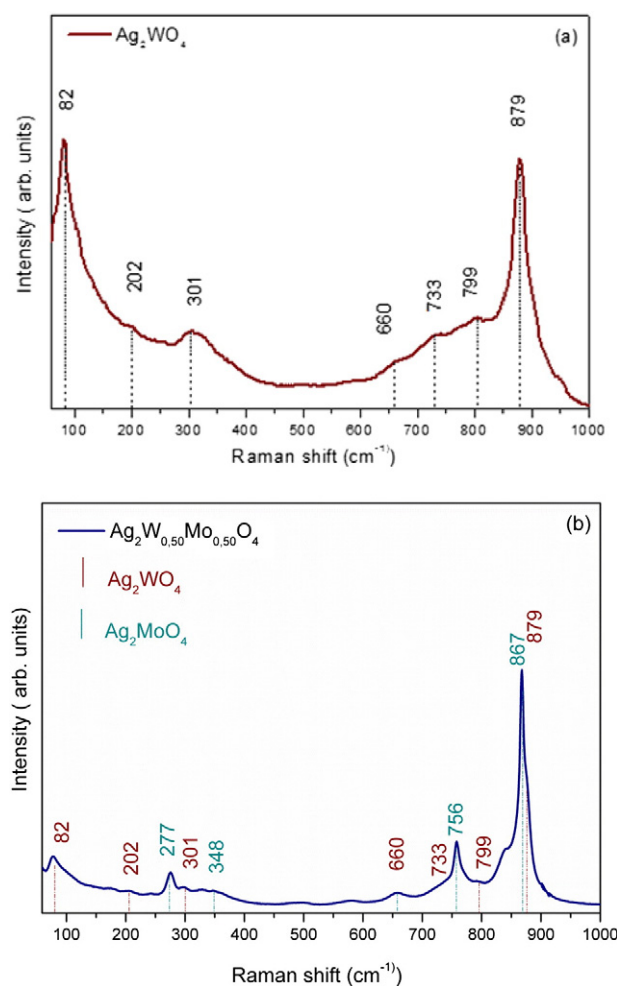| $Ag_2(W_{1-x}Mo_x)O_4$ | Phase 1 | Phase 2 | $\chi^2$ | $R_{Bragg}$ | $R_p$ | $R_{wp}$ |
|---|---|---|---|---|---|---|
| x = 0 | $Ag_2WO_4$ − 100% | – | 1.77 | 4.15 | 9.60 | 13.80 |
| x = 0.50 | $Ag_2W_{0.92}Mo_{0.08}O_4$ 67.15% | $Ag_2W_{0.08}Mo_{0.92}O_4$ 32.85% | 2.09 | 5.10 | 11.20 | 15.16 |

**Table 2**
Lattice parameters and unit cell volume obtained by Rietveld refinement for the $Ag_2(W_{1-x}Mo_x)O_4$ crystals with ($x = 0$ and 0.50) synthesized at 140 °C for 1 h by the MAH method.

| $Ag_2(W_{1-x}Mo_x)O_4$ | Phase 1 | | | | Phase 2 | |
|---|---|---|---|---|---|---|
| | Lattice parameters (Å) | | | Volume (Å$^3$) | Lattice parameters (Å) | Volume (Å$^3$) |
| | a | b | c | | a = b = c | |
| $x = 0$ | 10.887(1) | 12.015(4) | 5.890(3) | 770.525(3) | – | – |
| $x = 0.50$ | 10.834(5) | 12.035(6) | 5.906(0) | 770.13(5) | 9.325(8) | 811.079(2) |

of the diffuse reflectance measures, extracting the $E_{gap}$ values with good accuracy [31]. Therefore, this method can be used in the limiting case of an infinitely thick sample, as the thickness and sample holder have no effect on the reflectance (R) value. In this case, the Kubelka–Munk function at any wavelength is as follows:

$$F(R_\infty) = \frac{(1-R_\infty)^2}{2R_\infty} = \frac{k}{s} \qquad (2)$$

where $F(R_\infty)$ is the remission or Kubelka–Munk function, i.e., the diffuse reflectance of the layer relative to a non- or low-absorbing standard (MgO in our case), which is related to the term $R_\infty = R_{sample}/R_{MgO}$; $k$ is the molar absorption coefficient of the samples; and $s$ is the scattering coefficient.

The optical band gap and the absorption coefficient of a semiconductor oxide are calculated using Eq. (3):

$$\alpha h\nu = C_1 (h\nu - E_{gap})^n \qquad (3)$$

where $\alpha$ is the linear absorption coefficient of the material, $h\nu$ is the photon energy, $C_1$ is a proportionality constant, $E_{gap}$ is the optical band gap, and $n$ is a constant associated with the different types of electronic transitions. In this phenomenon, the electronic charges located in the maximum-energy states in the valence band enter the minimum-energy states in the conduction band after an absorption process, but they always occur in the same region of the Brillouin zone [32]. Based on this information, the $E_{gap}$ values for the $Ag_2(W_{0.5}Mo_{0.5})O_4$ crystals were calculated using the remission function presented in Eq. (2). Furthermore, by replacing the term $k$ with $2\alpha$, we obtain the modified Kubelka–Munk function as follows:

$$[F(R_\infty)h\nu]^2 = C_2 (h\nu - E_{gap}). \qquad (4)$$

Therefore, by obtaining $F(R_\infty)$ from Eq. (2) and plotting $[F(R_\infty)h\nu]^2$ against $h\nu$ and $C_2$ (proportionality constant), we can determine the $E_{gap}$ values of the compounds by extrapolating the linear portions of the curves.
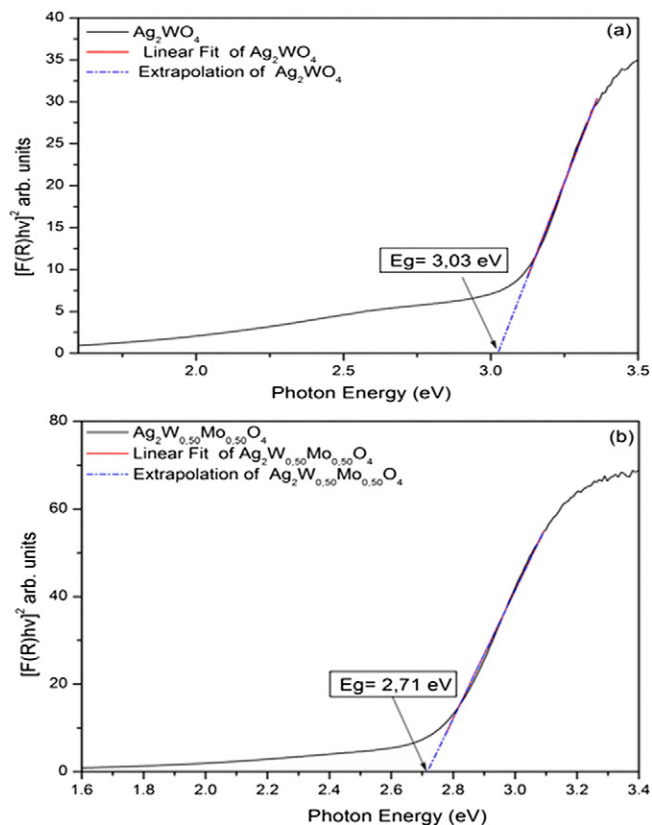


Fig. 3. FT-Raman spectra for $Ag_2(W_{1-x}Mo_x)O_4$ crystals with (a) x = 0 and (b) 0.50 synthesized at 140 °C for 1 h by the MAH method.



Fig. 4. UV–vis spectra for $Ag_2(W_{1-x}Mo_x)O_4$ crystals with (a) x = 0 and (b) 0.50 synthesized at 140 °C for 1 h by the MAH method.

Fig. 4(a–b) depict the UV–vis diffuse reflectance spectra of $Ag_2W_{1-x}Mo_xO_4$ (x = 0.0 and 0.50) crystals. The exponential optical absorption edge and the optical band-gap energy are controlled by the degree of structural disorder in the lattice. Thus, a replacement of W atoms by Mo atoms into the $Ag_2WO_4$ lattice is accompanied by the reduction of $E_{gap}$ values (Fig. 4 a–b). We believe that this significant reduction is attributable to intrinsic defects at the local range introduced by the presence of two network formers. The partial substitution of a network former induces a decrease of the band gap from 3.03 eV ($Ag_2WO_4$) to 2.71 eV ($Ag_2W_{0.50}Mo_{0.50}O_4$) and introduces new intermediary energy levels within the optical band gap. This effect results in distortions in the $[AgO_y]$, $[WO_6]$, and $[MoO_4]$ clusters that are interlinked in the lattice and causes the appearance of new intermediate electronic levels in the band gap. The decrease in the band gap can also be attributed to defects, local bond distortion, intrinsic surfaces states, and interfaces that yield these localized electronic levels in the forbidden band gap [33].

Our results for the values of the direct energy band gap for pure $Ag_2WO_4$ microcrystals agree well with those reported in the literature [34]. To our knowledge, the heterostructures and band-gap values obtained in this work ($Ag_2W_{0.5}Mo_{0.5}O_4$) have not previously been reported.

## 3.5. Photoluminescence emission of $Ag_2W_{1-x}Mo_xO_4$ crystals

Fig. 5 shows the PL emission spectra recorded at room temperature for the $Ag_2W_{1-x}Mo_xO_4$ samples (x = 0.0 and 0.50) excited at 350.7 nm. All the samples exhibited a broad band in the range of 300–600 nm with a maximum at the violet end (ca. 450.0 nm) of the visible spectrum.

The PL results show behavior typical of multiphonon or multilevel processes; i.e., a solid system where reactions occur by several pathways, which involve the participation of numerous energy states within the band gap [35]. PL is a powerful probe to investigate certain aspects of short- and medium-range orders for clusters in which the degree of local order is such that structurally different sites can be distinguished by modifications in electronic transitions that are linked to a specific structural arrangement [36].

The PL intensity of the $Ag_2W_{0.50}Mo_{0.50}O_4$ heterostructure presents an improvement over that of the pure $Ag_2WO_4$ compound (Fig. 5). Therefore, the maximum broad band related to the compound with $[MoO_4]$ clusters moves towards a lower energy region (400 nm) than that observed for the $Ag_2WO_4$ compound (450 nm). In addition, a weak contribution (diffuse emission) in the red region (~600–700 nm) appears for the $Ag_2WO_4$ sample, while the $Ag_2W_{0.50}Mo_{0.50}O_4$
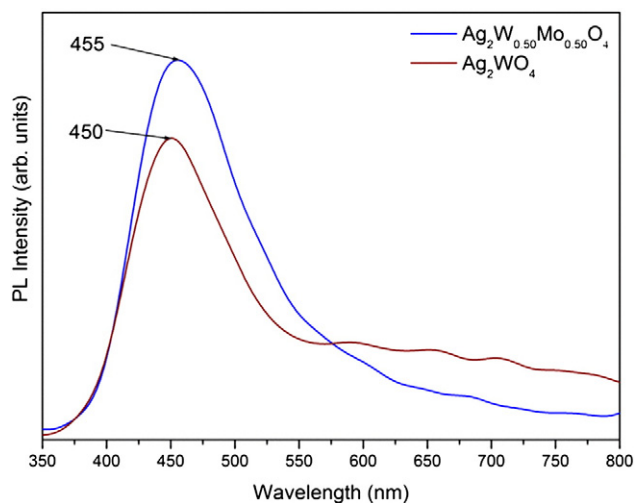
compound showed no emission in this wavelength region. According to Longo et al. [8], the emission in the red spectrum is most likely related to the $[AgO_y]$ clusters. In this manner, an increase in the violet PL emission in the $Ag_2W_{0.50}Mo_{0.50}O_4$ sample is also related to order–disorder effects, which significantly influence the luminescence properties of the tungstates [37].

The synergy between the two network formers results in a special structural condition associated with the appearance of stronger violet PL emissions. Other factors are involved in the PL behavior observed and include the degree of aggregation and orientation between particles, variations in the particle size distribution, and surface defects. All these factors greatly influence the intensity of PL emission. In addition, distortions on $[AgO_y]$, $[WO_6]$, and $[MoO_4]$ clusters at the local range and morphology changes can be considered other key factors responsible for the emission profiles of this $Ag_2WO_4$ matrix. Therefore, theoretical calculations are required to gain further insight into the possible mechanisms.

De Santana et al. [33] prepared a core/shell structure with silver tungstate and silver molybdate composites. They reported an enhancement of the PL spectrum for the decorated sample attributable to the presence of an $Ag_2MoO_4$ shell covering the surface of the $\alpha$-$Ag_2WO_4$ core.

In another work [38], a heterostructure composite formed by two semiconductors was recognized as promising for the development of a new, efficient material. According to the authors, heterostructures can promote efficient electron–hole separation and, thus, improve the physical and chemical properties compared to those of a single semiconductor [39]. Kong et al. [40] synthesized $BiOBr$–$ZnFe_2O_4$ heterostructures, which were found to exhibit higher photocatalytic activity in the visible-light degradation of rhodamine B than single $BiOBr$ and $ZnFe_2O_4$.

## 3.6. FE-SEM analyses

Fig. 6(a–b) shows FE-SEM images of $Ag_2W_{1-x}Mo_xO_4$ (x = 0.0 and 0.50) crystals synthesized by the co-precipitation method. Fig. 6(a) shows several rod-like, elongated, agglomerated $Ag_2WO_4$ microcrystals with a polydisperse shape. The image reveals that the crystals are large and irregular with diameters of ~3 μm. This morphology may be attributed to the growth mechanism of the crystal during the precipitation reaction. The formation of $Ag_2WO_4$ nuclei occurs when the solution containing $Ag^+$ ions comes into contact with the solution containing $WO_4^{2-}$ ions, with the subsequent aggregation of several nuclei to form $Ag_2WO_4$ crystals. After some time, these original crystals grow to form rod-like structures. The last drops of the solution containing $WO_4^{2-}$ ions tend to form smaller crystals. Then, new nucleation events can occur. These events are characterized by the appearance of small crystals that have not yet grown because they have been formed at the end of the precipitation reaction and lack further material for growth by the drop-by-drop methodology [41]. This nucleation is heterogeneous; i.e., when a drop falls, some nuclei are formed while other nuclei grow simultaneously. At this stage, random collisions may still occur. On the other hand, some smaller rod-like crystals may possibly have been formed after the dissolution of some larger crystals under hydrothermal conditions.

When $MoO_4^{2-}$ ions were simultaneously added to the co-precipitation reaction of $Ag_2WO_4$, it was found that the morphologies of the final products greatly changed. Fig. 6(b) shows an FE-SEM image of the $Ag_2W_{0.5}Mo_{0.5}O_4$ crystals. These crystals are formed by the self-assembly of several nanocrystals partially oriented with each other and have an average size of approximately 3–5 μm. The growth tendency of double-structure microcrystals is clear, as shown in the heterostructure crystals $Ag_2WO_4$/$Ag_2MoO_4$ in Fig. 6(b). When the Mo ions were added to the reaction mixture, we can observe the presence of rounded microcrystals corresponding to the $Ag_2MoO_4$ phase reported in the literature. Therefore, the morphology changes depend on the presence of Mo. Recent attention has been focused on the synthesis and application of heterostructure compounds,
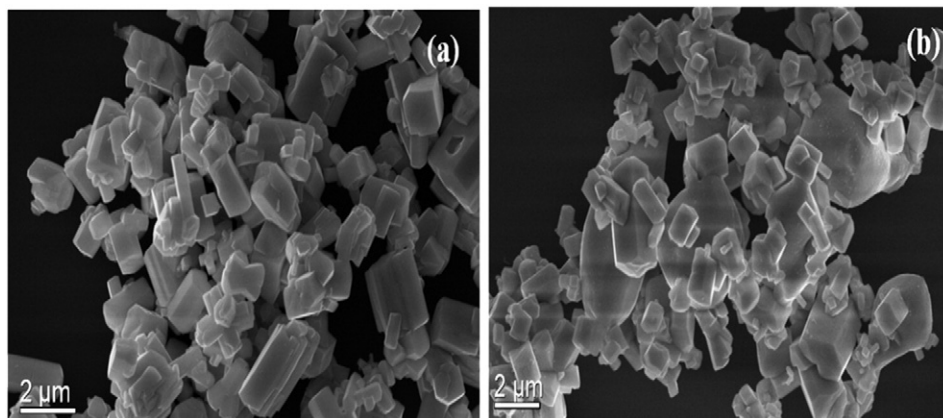


**Fig. 5.** PL emission for $Ag_2(W_{1-x}Mo_x)O_4$ crystals (with x = 0 and 0.50) synthesized at 140 °C for 1 h by the MAH method.

Fig. 6. FE-SEM images of $Ag_2(W_{1-x}Mo_x)O_4$ crystals with (a) x = 0 and (b) 0.50 synthesized at 140 °C for 1 h by the MAH method.

which can have superior performance compared to single-structured materials [42].

In situ electron microscopy is an important technique that can uncover dynamic processes in the growth of nanocrystals. Recent technological advancements, in conjunction with high-resolution imaging, provide a new opportunity to view nanoscale processes [43]. In Fig. 7(b), we can observe silver filaments on the $Ag_2W_xMo_xO_4$ (x = 0.0, 0.50) crystals driven by an accelerated electron beam from an electronic microscope under high vacuum at different exposure times. (DRX) and Raman analysis (Figs. 1 and 2) were incapable of detecting any significant change in the $Ag_2W_{1-x}Mo_xO_4$:Ag samples. In contrast, the FE-SEM images (Fig. 7(b)) reveal that after receiving a small

electron dose, the $Ag_2W_xMo_xO_4$ (x = 0.0, 0.50) crystal surface contains a small amount of Ag nanoparticles. After 5 min of exposure to a 10-kV electron beam, the metallic Ag nanoparticles begin to grow on the sample surface. This reduction process converts $[AgO_y]$ clusters to $Ag^0$. Longo et al. [33] demonstrated the similar behaviors of growth processes of Ag filaments on $\alpha$-$Ag_2WO_4$ crystals induced by electron-beam irradiation by using electron microscopy. They postulated that after irradiation, the growth of the first Ag particles and the onset of the growth of new nuclei were observed in all the samples heat treated at different temperatures (100, 120, 140 and 160 °C). However, the sample prepared at 160 °C shows a higher number of Ag nuclei as well as a higher absorption of existing particles. In another work [44], our
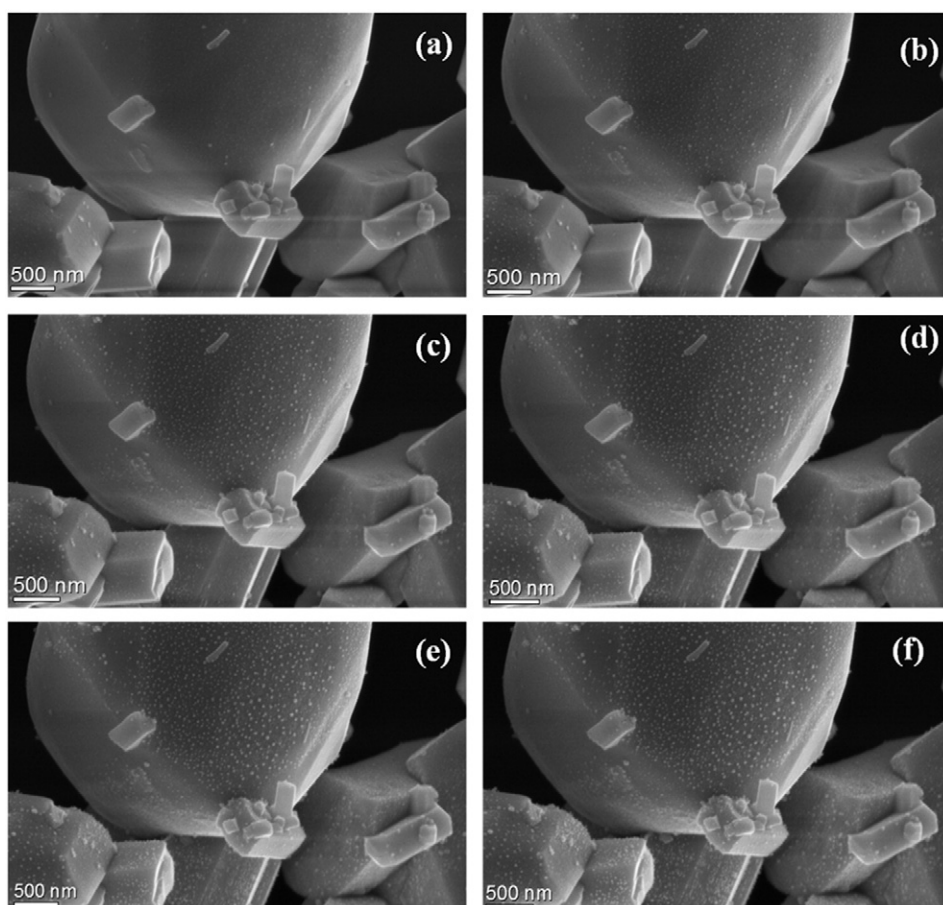


Fig. 7. FE-SEM images of $Ag_2W_{0.50}Mo_{0.50}O4$ crystals after electron beam exposure for different times (a) 0 min, (b) 1 min, (c) 2 min, (d) 3 min, (e) 4 min and (f) 5 min.

group proposed the antibacterial effect of $Ag_2WO_4$ microcrystals with Ag metallic nanofilaments obtained by irradiation, employing an electron beam to combat planktonic cells of methicillin-resistant *Staphylococcus aureus* (MRSA). Experimental data and theoretical calculations suggest that this effect originates from the coupling between $\alpha$-$Ag_2WO_4$ and Ag and promotes electron and hole transfer processes that can readily participate in anti-microbacterial processes.

Fig. 8 shows an FE-SEM image showing Ag nanoparticles on the surface of the $Ag_2W_xMo_xO_4$ compound after 5 min of exposure to a 10-kV electron beam as well as the size distribution of silver nanoparticles. The sizes of the irradiated Ag nanoparticles vary from 17–79 nm with a distribution maximum at approximately 28 nm (Fig. 8(b)). The formation of silver nanoparticles of similar sizes was observed by Pereira et al. [45], who investigated the formation and growth of silver on $\alpha$-$Ag_2WO_4$ at different times and with different chemical compositions, size distributions, and element distributions. The diameters of most Ag particles were in the range of 20–40 nm. In this work, the injection of electrons decreases the activation barrier for the Ag diffusion process, and the formation of Ag nanoparticles is not dependent on the electron-beam voltage.

## 4. Conclusion

$Ag_2W_{0.50}Mo_{0.50}O_4$ crystals were successfully grown with the MAH method. We observed the partial replacement of $WO_6$ clusters by $MoO_6$ clusters and vice versa. These results suggest that the combination of silver tungstates and molybdates results in heterostructures with interesting morphologies showing PL performance superior to

that of single-structured $Ag_2WO_4$. An electron-irradiation process strongly affects the nucleation and growth of Ag filaments and can provide deep insight into the electronic structure of other silver-oxide-based materials. Moreover, the present work can be used to explore the potential of Ag nanoparticles for use in various applications.

## References

[1] M. Feng, M. Zhang, J.M. Song, X.G. Li, S.H. Yu, ACS Nano 5 (2011) 6726–6735.
[2] E.K. Fodjo, D.W. Li, N.P. Marius, T. Albert, Y.T. Long, J. Mater. Chem. A 1 (2013) 2558–2566.
[3] X. Liu, J. Hu, J. Li, Y. Hu, Y. Shao, H. Yang, G. Tong, H. Qian, Mater. Lett. 91 (2013) 129–132.
[4] E. Wenda, J. Therm. Anal. 36 (1990) 1417.
[5] S.A. Suthanthiraraj, Y.D. Premchand, Ionics 10 (2004) 254–257.
[6] L. ZhaoQian, C. XueTai, X. Zi-Ling, Sci. China Chem. 56 (2013) 443–450.
[7] E. Longo, L.S. Cavalcante, D.P. Volanti, A.F. Gouveia, V.M. Longo, J.A. Varela, M.O. Orlandi, J. Andre, Sci. Rep. 3 1676 (2013) 1–4.
[8] E. Longo, D.P. Volanti, V.M. Longo, L. Gracia, I.C. Nogueira, M.A.P. Almeida, A.N. Pinheiro, M.M. Ferrer, L.S. Cavalcante, J. Andres, J. Phys. Chem. C 118 (2014) 1229–1239.
[9] X. Wang, C. Fu, P. Wang, H. Yu, J. Yu, Nanotechnology 24 (2013) 1–8.
[10] A.J. Vandenberg, C.A.H. Juffermans, J. Appl. Crystallogr. 15 (1982) 114–116.
[11] R.R. Kharade, S.S. Mali, S.P. Patil, K.R. Patil, M.G. Gang, P.S. Patil, J.H. Kimand, P.N. Bhosale, Acta 102 (2013) 358–368.
[12] D.P. Dutta, A. Singh, A. Ballal, A.K. Tyagi, Eur. J. Inorg. Chem. 46 (2014) 5724–5732.
[13] L. Pan, L. Li, Y. Chen, J. Sol-Gel Sci. Technol. 66 (2013) 330–336.
[14] L.S. Cavalcante, M.A.P. Almeida, W. Avansi Jr., R.L. Tranquilin, E. Longo, N.C. Batista, V.R. Mastelaro, M. Siu Li, Inorg. Chem. 5 (2012) 10675–10687.
[15] L.F. da Silva, A.C. Catto, W. Avansi Jr., L.S. Cavalcante, J. Andres, K. Aguir, V.R. Mastelaro, E. Longo, Nanoscale 6 (2014) 4058–4062.
[16] E.Y. Liu, W.Z. Wang, Y.M. Gao, J.H. Jia, Tribol. Lett. 47 (2012) 21–30.
[17] P.M. Skarstad, S. Geller, Mater. Res. Bull. 10 (1975) 791–799.
[18] A.C. Larson, R.B. Von Dreele, General Structure Analysis System — GSAS, Los Alamos National Laboratory, copyright© 1985–2004, The Regents of the University of Califórnia, version 1.74, EUA, 2001.
[19] V. Nassif, R.E. Carbonio, J.A. Alonso, J. Solid State Chem. 146 (1999) 266–270.
[20] C. Bernuy-Lopez, M. Allix, C.A. Bridges, J.B. Claridge, M.J. Rosseinsky, Chem. Mater. 19 (2007) 1035–1043.
[21] P. Thompson, D.E. Cox, J.B. Hastings, J. Appl. Crystallogr. 20 (1987) 79–83.
[22] L.W. Finger, D.E. Cox, A.P. Jephcoat, J. Appl. Crystallogr. 27 (1994) 892–900.
[23] P.W. Stephens, J. Appl. Crystallogr. 32 (1999) 281–289.
[24] A.P.A. Marques, F.V. Motta, E.R. Leite, P.S. Pizani, J.A. Varela, E. Longo, D.M.A. de Melo, J. Appl. Phys. 104 (2008) 1–7.
[25] P.F.S. Pereira, A.P. de Moura, I.C. Nogueira, M.V.S. Lima, E. Longo, P.C. de Sousa, O.A. Serra, E.J. Nassar, I.L.V. Rosa, J. Alloys Compd. 526 (2012) 11–21.
[26] G. Nagaraju, G.T. Chandrappa, J. Livage, Bull. Mater. Sci. 31 (2008) 367–371.
[27] D. Stone, J. Liu, D.P. Singha, C. Muratore, A.A. Voevodin, S. Mishra, C. Rebholz, Q. Ge, S.M. Aouadi, Scr. Mater. 62 (2010) 735–738.
[28] A. Phuruangrat, T. Thongtem, S. Thongtem, J. Cryst. Growth 311 (2009) 4076–4081.
[29] A. Phuruangrat, T. Thongtem, S. Thongtem, J. Phys. Chem. Solids 70 (2009) 955–959.
[30] P. Kubelka, F. Munk-Aussig, Ein Beitrag zur Optik der Farbanstriche, Z. Tech. Phys. 12 (1931) 593–601.
[31] A.E. Morales, E.S. Mora, U. Pal, Rev. Mex. Fis. 53 (2007) 18–22.
[32] R.A. Smith, Semiconductors, 2nd ed. Cambridge University Press, London, 1978 434.
[33] Y.V.B. De Santana, J.E.C. Gomes, L. Matos, G.H. Cruvinel, A. Perrin, C. Perrin, J. Andrès, J.A. Varela, E. Longo, Nanomater. Nanotechnol. 4 (2014) 1–10.
[34] W.F. Zhang, Z. Yin, M.S. Zhang, Z.L. Du, W.C. Chen, J. Phys. Condens. Matter 11 (1999) 5655–5660.
[35] V.M. Longo, L.S. Cavalcante, E.C. Paris, J.C. Sczancoski, P.S. Pizani, M.S. Li, J. Andres, E. Longo, J.A. Varela, J. Phys. Chem. C 115 (2011) 5207–5219.
[36] V.M. Longo, E. Orhan, L.S. Cavalcante, S.L. Porto, J.W.M. Espinosa, J.A. Varela, E. Longo, Chem. Phys. 334 (2007) 180–188.
[37] L.S. Cavalcante, F.M.C. Batista, M.A.P. Almeida, A.C. Rabelo, I.C. Nogueira, N.C. Batista, J.A. Varela, M.R.M.C. Santos, E. Longo, M. Siu Li, RSC Adv. 2 (2012) 6438–6454.
[38] Z. Zhang, W.Z. Wang, L. Wang, S.M. Sun, ACS Appl. Mater. Interfaces 4 (2012) 593–597.
[39] C. Ye, M.D. Regulacio, S.H. Lim, S. Li, Q.H. Xu, M.Y. Han, Chem. Eur. J. 21 (2015) 9514–9519.
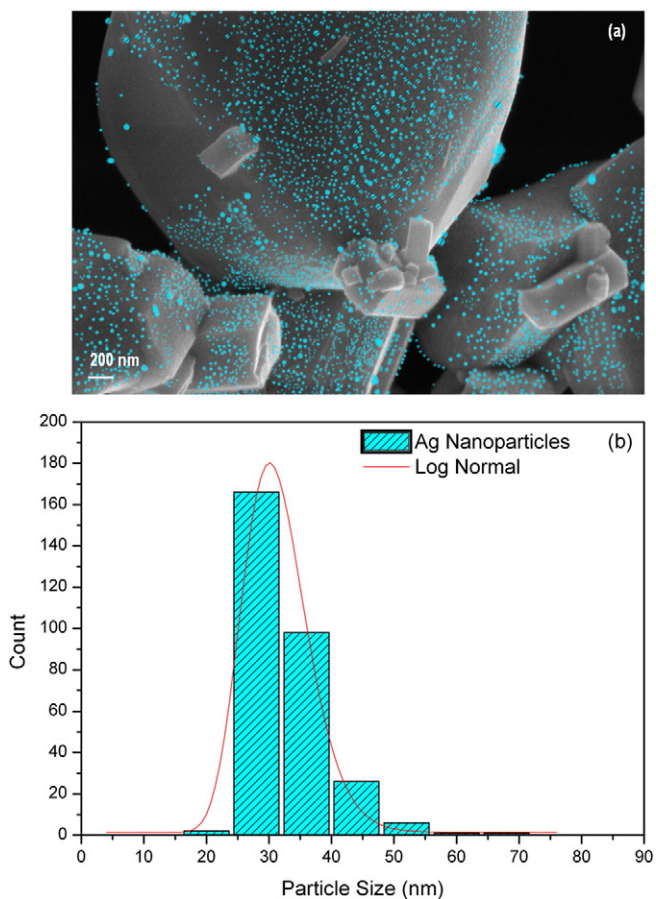[40] L. Kong, Z. Jiang, T.C. Xiao, L.F. Lu, M.O. Jones, P.P. Edwards, Chem. Commun. 47 (2011) 5512–5514.



**Fig. 8.** FE-SEM image of $Ag_2W_{0.50}Mo_{0.50}O4$ crystals (a) after 5 min electron beam exposure (b) mean particle diameter distribution for Ag nanoparticles.

[41] I.C. Nogueira, L.S. Cavalcante, P.F.S. Pereira, M.M. de Jesus, J.M. Rivas, Mercury, N.C. Batista, M. Siu Li, E. Longo, J. Appl. Crystallogr. 46 (2013) 1434–1446.

[42] L.Q. Mai, F. Yang, Y.L. Zhao, X. Xu, L. Xu, Y.Z. Luo, Nat. Commun. 381 (2011) 1637–1639.

[43] C. Scaiano, K. Stamplecoskie, J. Phys. Chem. Lett. 4 (2013) 1177–1187.

[44] V.M. Longo, C.C. De Foggi, M.M. Ferrer, A.F. Gouveia, R.S. André, W. Avansi, C.E. Vergani, A.L. Machado, J. Andrés, L.S. Cavalcante, A.C. Hernandes, E. Longo, J. Phys. Chem. A 118 (2014) 5769–5778.

[45] W.D.S. Pereira, J. Andres, L. Gracia, M.A. San-Miguel, E.Z. da Silva, E. Longo, V.M. Longo, Phys. Chem. Chem. Phys. 17 (2015) 5352–5535.